



Enhanced azo dye decolorization through charge transmission by σ -Sb³⁺-azo complexes on amorphous Sb₂S₃ under visible light irradiation

Fan Li^{a,c}, Lili Zhang^a, Chun Hu^{b,*}, Xueci Xing^b, Bing Yan^b, Yaowen Gao^b, Li Zhou^b

^a Key Laboratory of Drinking Water Science and Technology, Research Center for Eco-Environmental Sciences, Chinese Academy of Sciences, Beijing 100085, China

^b Key Laboratory for Water Quality and Conservation of the Pearl River Delta, Ministry of Education, Institute of Environmental Research at Greater Bay, Guangzhou University, Guangzhou 510006, China

^c University of Chinese Academy of Sciences, Beijing 100049, China



ARTICLE INFO

Keywords:

Amorphous Sb₂S₃
Visible light
Photocatalysis
Azo group
Adsorption
Complex

ABSTRACT

Three types of Sb₂S₃ with different degrees of crystallinity were synthesized via a hydrothermal procedure by adjusting the concentration of hydrochloric acid. The amorphous Sb₂S₃ sample (A-Sb₂S₃) exhibited nearly 13 times higher photocatalytic activity for the decolorization and biodegradability improvement of MO solution compared with both crystalline samples under visible light ($\lambda > 420$ nm). It was verified that MO and Congo Red azo dyes were adsorbed onto A-Sb₂S₃ by displacing hydroxyl groups (OH⁻) to complex with Sb³⁺ on A-Sb₂S₃, which occurred via σ bonding to the lone pairs of azo nitrogen atoms with Sb³⁺ (σ -Sb-(N=N-)). Moreover, the decolorization rate of MO was positively related to its adsorption onto A-Sb₂S₃, and no significant degradation was observed for non-azo intermediates. The predominant photodegradation pathways of MO were reduction and oxidization to sulfanilic acid, NO₃⁻ and small-molecule acids. On the basis of photoelectron spectra, ESR (Electron spin resonance) measurements and other experimental information, it was proposed that the complexes (σ -Sb-(N=N-)) could transmit photogenerated electrons and holes to the azo group, breaking the N=N bond, causing azo dye decolorization to improve their biodegradability; while on the surface of bare A-Sb₂S₃, the strong coordination interaction of OH⁻ with Sb³⁺ made OH⁻ groups become the recombination centers for photogenerated electrons and holes during the photocatalytic reaction.

1. Introduction

In recent decades, wastewater treatment is becoming an increasingly serious issue, predominantly caused by rapid industrialization. The emission of azo dyes, whose structures contain aromatic rings linked together by an azo group (—N=N—), is undesirable [1]. Among the traditional technologies, adsorption and biological treatment are used to purify the wastewater. However, adsorption can only concentrate the pollutant rather than cause degradation, so that it needs further treatment; and biological treatment is inadequate for decolorization and degradation of azo dyes due to the existence of the azo group and aromatic ring structure [2,3], which are stable toward biological processes. Thus, developing an effective treatment technique for azo dye wastewater has attracted great research interest in the environmental field.

Semiconductor photocatalysis, in which inexhaustible and clean solar energy can be harvested as a potential resource, has been proved to be an effective and environmentally friendly pretreatment to achieve

the decolorization of azo dyes [2,4–7]. The photocatalytic mechanism for pollutant degradation mainly involves three steps: (i) light absorption to generate electron-hole pairs, (ii) charge separation and migration in the semiconductor, and (iii) surface chemical reactions between carriers and other compounds, or carrier recombination [8–10]. And based on this mechanism, extensive strategies have been explored, such as ion doping (B and N) [11,12], defect introduction [13,14], formation of heterostructures between two semiconductors [15,16], surface plasmonic enhancement (Ag and Au) [17,18] and crystalline facet engineering [19,20], which significantly improve the efficiency of light absorption, carrier separation and migration. Nevertheless, the reaction efficiency of the surface electron-hole pairs also depends on the surface properties of the material.

In many photocatalytic research studies, the surface hydroxyl groups are usually activated by holes to generate hydroxyl radicals [21,22], which will oxidize pollutants on the surface of catalysts or in solution. However, most of these studies neglect the surface interaction of the surface hydroxyl groups and pollutants. Some researchers have

* Corresponding author.

E-mail addresses: huchun@gzhu.edu.cn, huchun@rcees.ac.cn (C. Hu).

observed partial charge transfer upon formation of a Ag^+ -phenol cationic complex due to the cation- π interaction [23]. In recent research, our group reported on pollutant degradation processes predominantly occurring on the surface of a catalyst owing to the formation of σ -Cu-ligand complexes between the phenolic OH group and surface Cu in a heterogeneous Fenton system [24]. These results provided a new insight for photocatalysis that complexes formed between the photo-catalyst and pollutants could efficiently promote partial charge transfer.

Antimony sulfide (Sb_2S_3), a V–VI semiconductor, owing to its advantageous properties such as suitable optical bandgap (1.5–2.2 eV) [25], high thermoelectric power and suitable band alignment with other materials [26], has gained considerable attention in many fields such as lithium-ion batteries [27], sodium-ion batteries [28,29], solar cells [26,30], optical devices and photoelectronic devices [25] etc. As for photocatalysis, extensive strategies have been exploited to improve the photocatalytic properties of Sb_2S_3 . For example, many Sb_2S_3 materials with different morphologies have been prepared, such as hollow microspheres [31], microrods [32] and nanotubes [33], and constructing heterostructures with other semiconductors [34–37] or metal nanoparticles [31] has been another strategy to enhance the catalytic performance. However, the surface interaction between Sb_2S_3 materials and pollutants still deserves further study.

Herein, we report the preparation of three types of Sb_2S_3 with different degrees of crystallinity, via simply adjusting the concentration of hydrochloric acid during synthesis. It was found that the amorphous Sb_2S_3 sample thus prepared showed substantially enhanced visible light photocatalytic activity towards the decolorization and biodegradability of MO solution. More importantly, it is worth pointing out that the surface hydroxyls of Sb_2S_3 are stable but could be partially replaced by azo groups, which contributed to the formation of a complex of Sb_2S_3 and MO via linkage between Sb^{3+} and azo groups ($\text{-N}=\text{N}-$). This complex promoted the efficiency of charge separation and migration, which in turn accelerated the decolorization of azo dyes. Therefore, a mechanism for this charge separation and migration, based on the surface complex, was proposed.

2. Experimental section

2.1. Materials

Antimony chloride (SbCl_3) was purchased from Aladdin Industrial Corporation. Sodium sulfide nonahydrate ($\text{Na}_2\text{S}\cdot 9\text{H}_2\text{O}$), hydrochloric acid (HCl), Methyl Orange (MO), Congo Red and Sodium hydroxide (NaOH) were obtained from Sinopharm Chemical Reagent Co. 5-tert-Butoxycarbonyl-5-methyl-1-pyrroline-N-oxide (BMPO) was supplied by the Bioanalytical Lab (Sarasota, FL). All chemicals were at least analytical grade.

2.2. Synthesis of amorphous and crystalline Sb_2S_3

The amorphous Sb_2S_3 was synthesized by a simple hydrothermal procedure. Typically, 1.52 g antimony chloride (SbCl_3) and 2.4 g $\text{Na}_2\text{S}\cdot 9\text{H}_2\text{O}$ were separately dissolved into 50 mL HCl solution (4 M) and 100 mL NaOH solution (2 M) with vigorous magnetic stirring at 30 °C. The above-mentioned solutions were referred to as solution A and B, respectively. After stirring for 30 min, solution A was injected into solution B, and the color gradually changed to dark brown. Then, the mixture was kept stirring for another 1 h. Finally, the suspension was transferred to a 200 ml Teflon-lined autoclave and heated at 100 °C for 12 h. After the autoclave was naturally cooled to room temperature, a red Sb_2S_3 material labelled as A- Sb_2S_3 was separated by filtration, washed with deionized water several times, and dried at 60 °C for 6 h. Black crystalline samples were prepared by altering the concentration of the HCl solution to 6 M and 8 M, and were labelled as C- Sb_2S_3 -1 and C- Sb_2S_3 -2, respectively.

2.3. Characterization

Powder X-ray diffraction (XRD, Scintag-XDS-2000) patterns using Cu K α radiation ($\lambda = 1.540598 \text{ \AA}$) were used to confirm the phase composition and crystalline structure of the Sb_2S_3 samples. The morphology of the samples was characterized with a field emission scanning electron microscope (FESEM, Hitachi, SU8020). High-resolution transmission electron microscopy (HRTEM) images were recorded using a JEOL-2010 TEM with an acceleration voltage of 200 kV. X-ray photoelectron spectroscopy (XPS) was performed to obtain information on the surface chemical states via an AXIS-Ultra instrument using monochromatic Al K α radiation (225 W, 15 mA, 15 kV) and low-energy electron flooding for charge compensation. To compensate for surface charge effects, binding energies were calibrated using the C1s hydrocarbon peak at 284.80 eV. UV-vis diffuse reflectance spectroscopy (UV-vis DRS) data and UV-vis spectra were obtained using a Shimadzu UV-3900 recording spectrophotometer. The photoluminescence intensity of the prepared photocatalysts was characterized using a fluorescence spectrometer (Cary Eclipse). The BET surface area of samples and the pore size distribution were recorded by performing N_2 adsorption/desorption experiments using an ASAP 2020 HD88 analyzer. The concentrations of SO_4^{2-} and NO_3^- were measured by an ion chromatograph (ICS-2000). Electron spin resonance (ESR) tests were carried out by using a Bruker model ESP 300E electron paramagnetic resonance spectrometer. ATR-FTIR spectra of a suspension of A- Sb_2S_3 were obtained using a Nicolet 8700 infrared spectrometer with a ZnSe horizontal ATR cell.

Transient photocurrent response plots and EIS Nyquist analysis were obtained using a three-electrode quartz cell with a 0.1 M NaSO_4 electrolyte solution and an electrochemical system (CHI 660D electrochemical workstation) under a 100 W Xe lamp with a 420 nm cutoff filter. A 10 mg sample was dispersed in 1 mL Nafion solution (5 wt%) by 15 min sonication. 100 μL of the suspension was taken out and spread evenly onto the conductive surface of ITO conductive glass, which was dried in air to form the working electrode. A platinum wire and saturated calomel electrode (SCE) were employed as the counter and reference electrodes.

2.4. Photocatalytic activity

The photocatalytic activity of the catalysts was tested by observing the degradation of azo dyes such as MO and Congo Red under a 150 W arc lamp with a UV cutoff filter ($\lambda > 420 \text{ nm}$). The distance between reactor and lamp source was 10 cm. The incident light intensity was 2.25 mW cm^{-2} , which was measured with a radiometer (Photoelectric instrument Factory Beijing Normal University). In a typical procedure, 0.06 g photocatalyst and 60 mL MO aqueous solution (10 mg L^{-1}) were added into the photo-reactor. As for the degradation of Congo Red, 0.02 g photocatalyst and 60 mL aqueous Congo Red (40 mg L^{-1}) were added into the reactor with constant stirring. Prior to irradiation, the suspension was magnetically stirred for 30 min in the dark to reach adsorption-desorption equilibrium under ambient air conditions. At given time intervals, 4 mL suspension samples were taken out and filtered to remove the catalyst powders and examined at 464 nm for MO and 497 nm for Congo Red using a UV-vis spectrophotometer (UV-3900, Shimadzu). In addition, to investigate the stability and recyclability of the catalyst, the used A- Sb_2S_3 was collected by filtration followed by washing with deionized water at neutral pH and drying at room temperature for the next cycle. COD was measured by the potassium dichromate standard method and BOD_5 was measured by the international standard method.

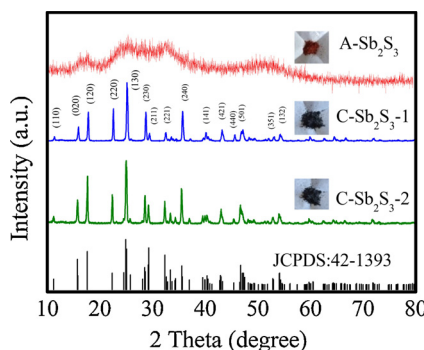


Fig. 1. XRD patterns of A-Sb₂S₃, C-Sb₂S₃-1, C-Sb₂S₃-2 samples.

3. Results and discussion

3.1. Structural characteristics

Fig. 1 shows the XRD patterns of amorphous Sb₂S₃ (A-Sb₂S₃) and crystalline Sb₂S₃ (C-Sb₂S₃-1 and C-Sb₂S₃-2). The XRD patterns of crystalline Sb₂S₃ (C-Sb₂S₃-1 and C-Sb₂S₃-2) with similar diffraction patterns could be well-indexed as the orthorhombic phase (JCPDS No. 42-1393) of Sb₂S₃. The intensity of some peaks varied, such as the (230) peak and (211) peak, indicating that the exposed surfaces of C-Sb₂S₃-1 and C-Sb₂S₃-2 were slightly different. No obvious characteristic peaks appeared in the XRD pattern of A-Sb₂S₃, indicating that amorphous Sb₂S₃ was formed in low-concentration HCl solution.

The FESEM and HRTEM images of the three types of Sb₂S₃ are shown in Fig. 2. For A-Sb₂S₃, Sb₂S₃ displayed an irregular aggregate morphology, which consisted of a great quantity of plate-like particles with rough surfaces (Fig. 2a₁). The HRTEM image of the A-Sb₂S₃ sample (Fig. 2a₂) did not show observable lattice fringes, suggesting that A-Sb₂S₃ was an amorphous material, consistent with the XRD result. The FESEM images of both C-Sb₂S₃-1 and C-Sb₂S₃-2 (Fig. 2b₁ and c₁) exhibited a rod-like morphology. It could be noted that there were more fragments surrounding the rods in the FESEM image of C-Sb₂S₃-1, which also led to the difference between the XRD patterns. And as shown in Fig. 2 b₂ and c₂, a distinct lattice fringe with an interplanar distance of 0.305 nm was observed, corresponding to the (211) plane of Sb₂S₃ (JCPDS 42-1393).

The BET specific surface area and pore structure of the as-prepared samples are shown in Fig. 3. A-Sb₂S₃ exhibited type IV isotherms and H₃ hysteresis loops [38], which are characteristic of slit-like pores and covered a broad relative pressure range of 0.75–1.00, illustrating the existence of mesopores and macropores (inset image of Fig. 3). Unlike A-Sb₂S₃, C-Sb₂S₃-1 and C-Sb₂S₃-2 showed type II isotherms and pores (inset image of Fig. 3), and the specific surface area of A-Sb₂S₃ (35.29 m² g⁻¹) was much larger than that of C-Sb₂S₃-2 (3.39 m² g⁻¹) and C-Sb₂S₃-1 (5.65 m² g⁻¹). The enhancement of the specific surface area could expose more active sites for the degradation of MO.

As shown in Fig. 4a, the two characteristic peaks for S 2p in A-Sb₂S₃ located at 163.28 eV and 162.11 eV were attributed to the binding energies of S 2p_{1/2} and S 2p_{2/3}, respectively. The two apparent symmetrical characteristic spin-orbit splittings of Sb 3d peaks at 539.55 eV and 530.26 eV were assigned to Sb 3d_{3/2} and Sb 3d_{5/2} (Fig. 4b), suggesting that antimony bound to sulfur remains in the Sb³⁺ oxidation state [25]. The result also confirmed that the A-Sb₂S₃ sample was a kind of amorphous Sb₂S₃, in agreement with its XRD pattern (Fig. 1).

The optical adsorption properties for the different samples are shown in Fig. 5a. The three samples all exhibited intense absorption bands in the UV and visible-light regions. As the concentration of the HCl solution decreased, the Sb₂S₃ sample changed from a dark color to red, (Fig. 1) and the absorption edge showed a blue-shift compared to

that of C-Sb₂S₃. The energy band gaps (E_g) of the as-prepared samples were also calculated according to the equation (Eq. (1)) [39,40]:

$$\alpha h\nu = A(h\nu - E_g)^{n/2} \quad (1)$$

where A, E_g, h and ν represent a proportionality constant, band gap, Planck constant, absorption coefficient and light frequency, respectively. While n is equivalent to 4 for indirect band gap materials, n = 1 for direct band gap materials like Sb₂S₃. It can be seen from Fig. 5b that the bandgap energies of C-Sb₂S₃-2, C-Sb₂S₃-1 and A-Sb₂S₃ were determined to be 1.50, 1.54, 1.83 eV, respectively. A-Sb₂S₃ had a wider bandgap than the crystalline materials (C-Sb₂S₃-2 and C-Sb₂S₃-1), which could prevent the excessive combination of carriers and facilitate the degradation of pollutants. In addition, compared with the C-Sb₂S₃ samples, A-Sb₂S₃ exhibited more intense visible light absorption (420–600 nm), which could be attributed to multiple reflections of the incident light within slit-like pores [41], and could be expected to show better photocatalytic performance.

In order to further demonstrate the optical and photoelectric properties, the transient photocurrent response, electrochemical impedance spectra (EIS) and photoluminescence (PL) spectra were measured, and the results are shown in Fig. 6. The transient photocurrent intensity of A-Sb₂S₃ reached values 2.8 and 1.7 times larger than those of C-Sb₂S₃-2 and C-Sb₂S₃-1 (Fig. 6A), indicating that photogenerated electrons and holes could be efficiently separated and rapidly transferred in A-Sb₂S₃. In addition, from the electrochemical impedance spectroscopy (EIS) measurements shown in Fig. 6B, it could be seen that the arc radius varied in the order A-Sb₂S₃ < C-Sb₂S₃-1 < C-Sb₂S₃-2, suggesting that A-Sb₂S₃ exhibited much smaller electrical resistance than the crystalline Sb₂S₃ samples and facilitated charge transfer. Furthermore, a weaker PL intensity means a lower electron-hole recombination rate, because the recombination of photo-generated electron/hole pairs can release energy in the form of fluorescence emission. Compared with C-Sb₂S₃-1 and C-Sb₂S₃-1, the PL emission intensity of A-Sb₂S₃ dramatically decreased at the excitation wavelength of 370 nm, indicating that amorphous Sb₂S₃ could effectively suppress the recombination of photogenerated charges and prolong the lifetime of photogenerated carriers to enhance the photocatalytic performance (Fig. 6C). The analysis result was consistent with the narrow light absorption region and wide bandgap of amorphous Sb₂S₃ observed in the UV-vis diffuse reflectance spectrum (Fig. 5). All the above results showed that the amorphous Sb₂S₃ material could promote the separation and transmission of photogenerated charges and inhibit their recombination efficiently.

3.2. Photocatalytic activity under visible light irradiation

To demonstrate the photocatalytic activity and stability of the catalysts, the degradation of MO was investigated in different sample suspensions under visible-light irradiation ($\lambda > 420$ nm). As shown in Fig. 7a, almost no obvious MO decomposition could be observed under visible light irradiation in the absence of a photocatalyst, suggesting that degradation by direct photolysis could be ignored. In the C-Sb₂S₃-1 suspension, the concentration of MO was only reduced by ca. 24% under visible light irradiation within 16 min. C-Sb₂S₃-2 showed slightly increased MO removal efficiency of ca. 44% within the same time. In addition, N-TiO₂ did not exhibit significant photocatalytic activity under the same condition. It is worth noting that A-Sb₂S₃ could achieve the complete decolorization of MO under otherwise identical conditions. In addition, a linear relationship between $-\ln(C/C_0)$ and reaction time (t) was observed, suggesting that the kinetics of the photo-degradation reaction of MO followed pseudo-first-order kinetics.

$$-\ln(C/C_0) = kt \quad (2)$$

where C and C₀ represent the concentration of MO solution at reaction time t and 0, respectively, and k is the pseudo-first-order constant

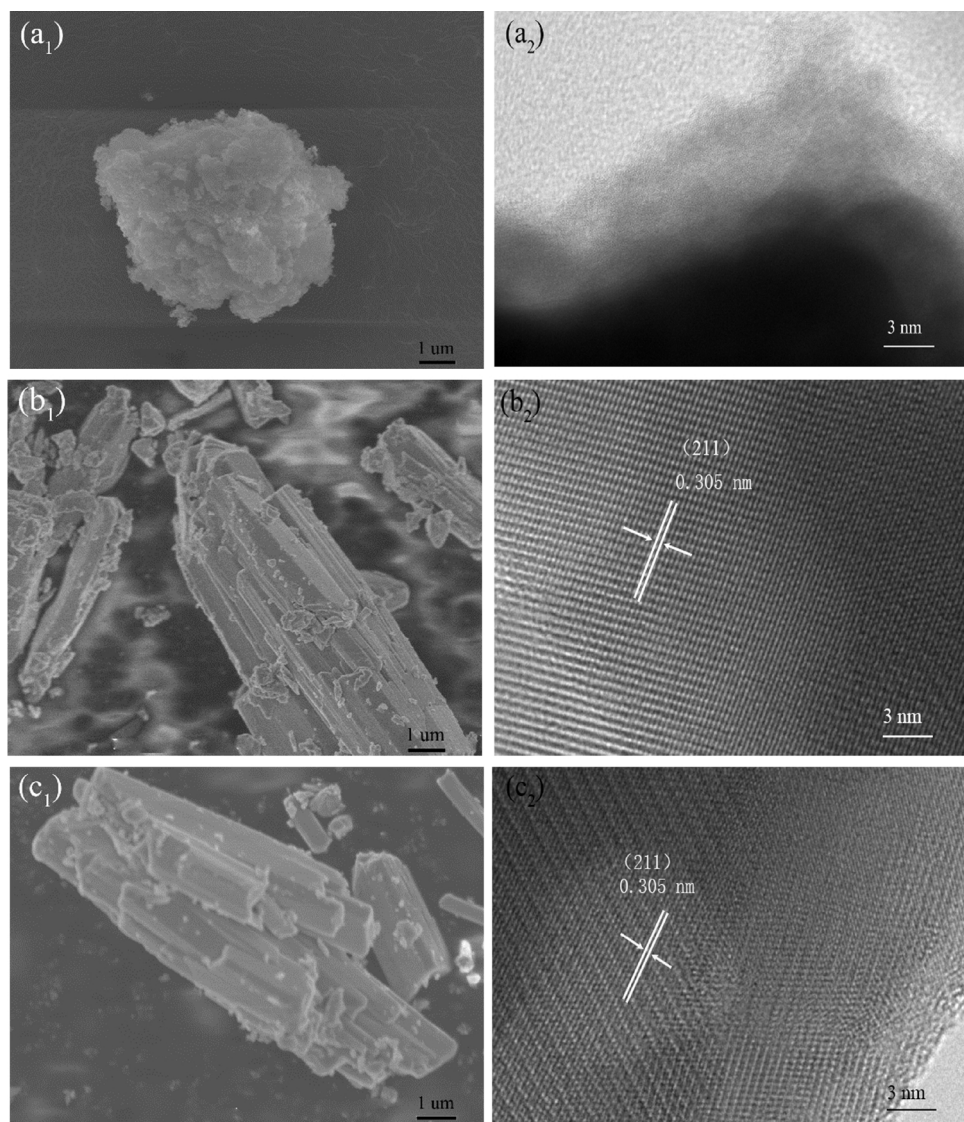


Fig. 2. FESEM images of A-Sb₂S₃ (a₁), C-Sb₂S₃-1 (b₁) and C-Sb₂S₃-2 (c₁); HRTEM images of A-Sb₂S₃ (a₂), C-Sb₂S₃-1 (b₂) and C-Sb₂S₃-2 (c₂).

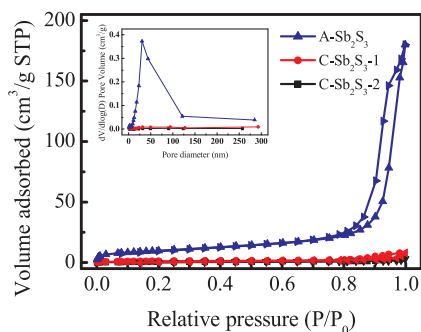


Fig. 3. N₂ adsorption/desorption isotherms and pore size distributions (inset) of different samples.

(min⁻¹). As illustrated in Fig. 7b, the sample A-Sb₂S₃ exhibited the highest photocatalytic efficiency ($k = 0.1848 \text{ min}^{-1}$), which was 12.7 times and 5.18 times higher than the values for C-Sb₂S₃-2 and C-Sb₂S₃-1 ($k = 0.0145 \text{ min}^{-1}$ and 0.0357 min^{-1}). The above results revealed that the amorphous Sb₂S₃ exhibited remarkably improved visible light photocatalytic performance. On the one hand, the amorphous Sb₂S₃ possessed a larger specific surface area and slit-like pores. On the other hand, when the Sb₂S₃ sample turned from a dark color to red (Fig. 1), it

exhibited a wider bandgap and more intense visible light absorption (420–600 nm). Ultimately, these changes exposed more active sites and enhanced the separation and migration efficiency of the electron-hole pairs.

The ratio of BOD₅/COD can be used to represent the biodegradability of the MO solution. Only when the ratio of BOD₅/COD is more than 0.3 can the water sample be biodegraded well. After 16 min of reaction, the ratio of BOD₅/COD increased from 0.18 to 0.42, suggesting that the biodegradability of MO was enhanced under the visible light irradiation.

Additionally, a recycling experiment for A-Sb₂S₃ is illustrated in Fig. 7c. It can be seen that during the 5 test cycles, the degradation of MO within 16 min was 97%, 91%, 90%, 88% and 85%, respectively. Actually, if the reaction time was extended to 25 min, the degradation of MO could still reach 98% in all cases, which indicated that the as-prepared A-Sb₂S₃ showed excellent catalytic stability for efficient decomposition of MO.

3.3. Photodegradation pathway of MO

As shown in Fig. 8a, the variation of the UV-vis absorption spectra of MO was measured for different reaction times in the A-Sb₂S₃ suspension. The conjugated structure from the azo group generated strong

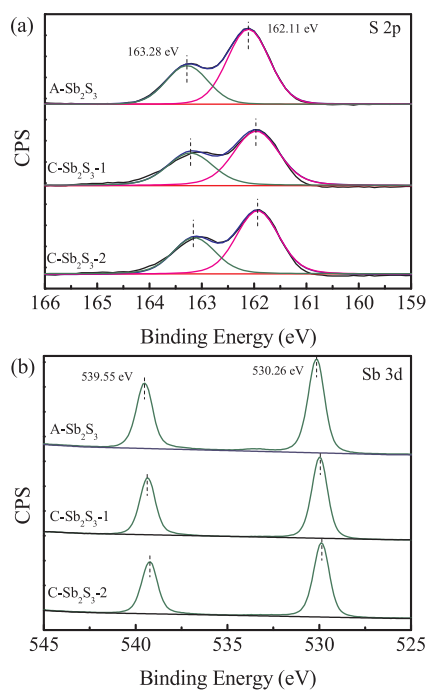


Fig. 4. XPS spectra of Sb₂S₃: (a) S 2p, (b) Sb 3d.

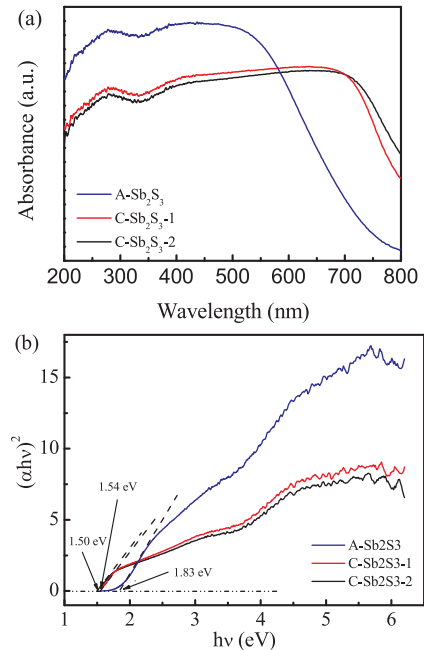


Fig. 5. UV-vis diffuse reflectance spectra (a) and Plots of $(\alpha h\nu)^2$ versus photon energy ($h\nu$) for the band gap energies of as-synthesized A-Sb₂S₃, C-Sb₂S₃-1 and C-Sb₂S₃-2 samples.

absorbance peaks at 464 nm and 270 nm ascribed to the $\pi \rightarrow \pi$ transition in the aromatic rings [42]. The characteristic peak intensities of MO gradually disappeared within 16 min irradiation time and a new peak at 250 nm appeared, which was related to sulfanilic acid [43]. The variation of the sulfanilic acid concentration was further determined by UV-vis spectroscopy, and the concentrations of NO⁻ and SO₂⁻ were also measured by ion chromatography during the degradation of MO. When 10 mg L⁻¹ MO is totally converted to sulfanilic acid, NO⁻ and other small-molecule acids, the theoretical final concentrations of sulfanilic acid and NO⁻ are 5.29 mg L⁻¹ and 3.79 mg L⁻¹. As shown in Fig. 8b, the concentrations of sulfanilic acid and NO⁻ quickly reached

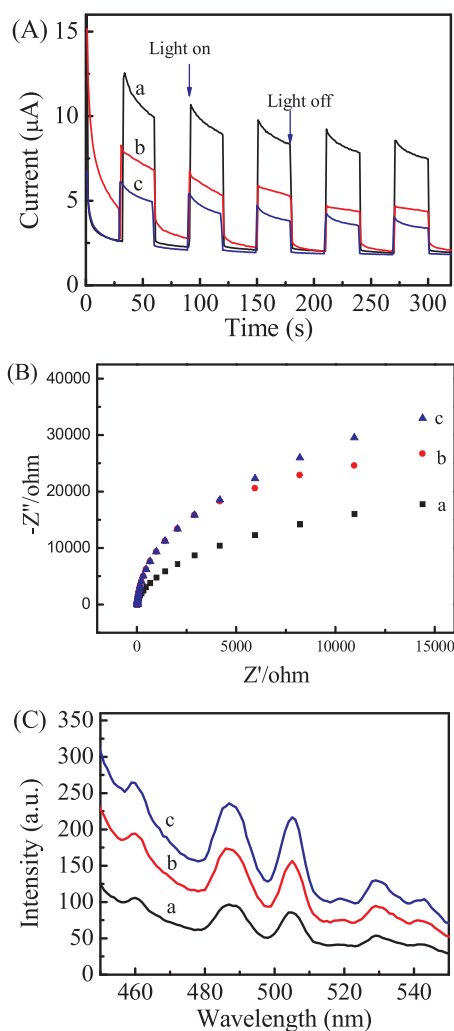


Fig. 6. (A) The transient photocurrent response, (B) EIS Nyquist plots and (C) Photoluminescence spectra of A-Sb₂S₃, C-Sb₂S₃-1 and C-Sb₂S₃-2 under visible light ($\lambda > 420$ nm) irradiation. (a) A-Sb₂S₃, (b) C-Sb₂S₃-1 and (c) C-Sb₂S₃-2.

5.19 mg L⁻¹ and 3.70 mg L⁻¹ within 16 min at almost the same rate. These results indicated that MO was decolorized through the breakage of the azo band, and sulfanilic acid and NO⁻ intermediates were produced. To further confirm the time variation of the azo group ($-N=N-$) and SO₂⁻ concentrations, MO solutions withdrawn at different reaction times were dried at low temperature and freeze-dried in vacuum to obtain FTIR spectra. As shown in Fig. 8c, the peaks of fresh MO at 1519 cm⁻¹ and 1038 cm⁻¹ were assigned to the azo group ($-N=N-$) and the asymmetric stretching vibration of the $-SO_3Na$ group [44]. From 0 min to 16 min, the band of the azo group ($-N=N-$) gradually disappeared, while the band of $-SO_3Na$ did not show any apparent change, which was also in agreement with the ion concentration measurements. As shown in Fig. 8b, TOC of the MO solution was slightly decreased in the A-Sb₂S₃ suspension for the dark reaction and then returned to the original value with the decolorization of MO under visible light irradiation, indicating that the intermediates could not be further oxidized. Therefore, a potential photocatalytic MO degradation pathway was proposed, as illustrated in Fig. 9. The product characterization proved that the photocatalytic degradation of MO predominantly involved (i) reduction of the azo group and generation of sulfanilic acid, (ii) oxidation of the azo group and the generation of NO⁻ and small-molecule acids.

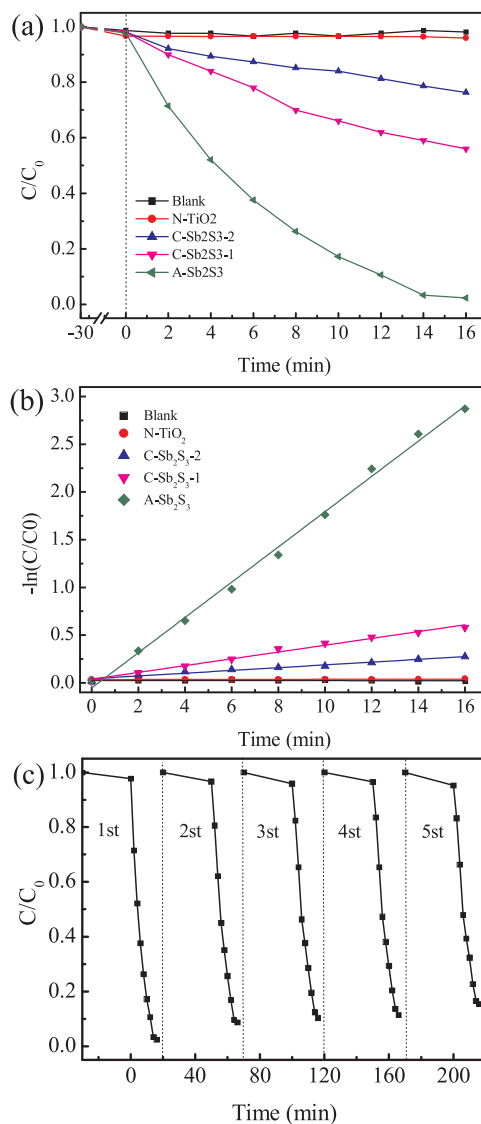


Fig. 7. (a) Degradation curves of MO and (b) $-\ln(C/C_0)$ versus reaction time of MO with different samples; (c) Cycling runs of A-Sb₂S₃ for the photocatalytic degradation of MO.

3.4. Complexing mechanism of Sb₂S₃ and MO

The effect of pH on the adsorption and photocatalytic degradation of MO is shown in Fig. 10. With pH decreasing from 8 to 2, the amount of MO adsorbed on the catalyst surface increased from 2.8% to 39%, correspondingly. The decolorization rate of MO was also significantly increased (Fig. 10a). Nevertheless, the TOC of the reaction solution was quickly restored to the initial value within 2 min and remained constant over 2 h (Fig. 10b), revealing that the intermediates could not be adsorbed onto the surface of the catalyst and further mineralized. The results suggested that MO first adsorbed on the surface of catalyst by the azo group ($-N=N-$) and was then degraded with visible light irradiation, and the intermediate products desorbed from the surface of Sb₂S₃ so that no further reaction occurred.

To further elucidate the role of the azo group in the degradation of pollutants, the photodegradation of Congo red (40 mg L^{-1}) containing two azo groups was carried out in the same system. As shown in Fig. 10c, after 30 min reaction in the dark, the adsorption amount of Congo red was 55% on the surface of Sb₂S₃, which was due to the presence of two azo groups in Congo Red. Even though the initial concentration of Congo Red was 40 mg L^{-1} , the complete

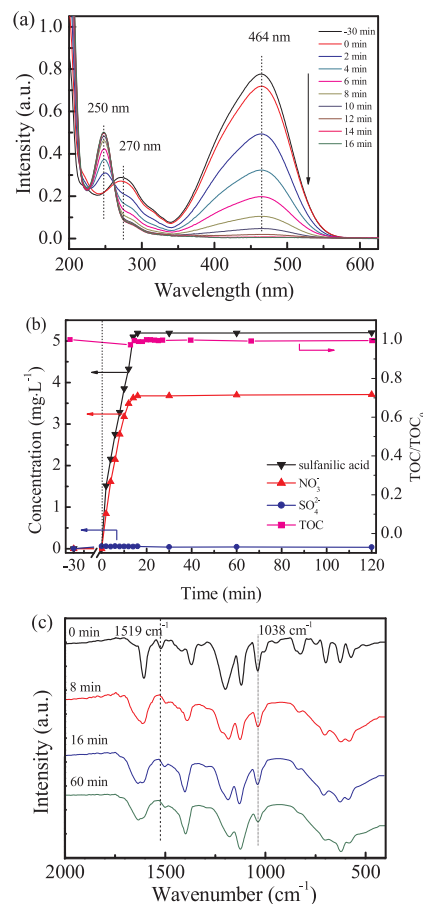


Fig. 8. (a) UV-vis spectra of MO samples, (b) The concentration of SO_4^{2-} , sulfanilic acid, NO_3^- taken during the photocatalytic process in the presence of A-Sb₂S₃ under visible light irradiation. (c) FTIR spectra for MO at different reaction times: 0, 8, 16, 60 min.

decolorization of Congo Red could still be achieved in 30 min. The TOC of Congo Red could be restored to the initial value within 15 min, which was similar to the results for MO. When the two azo groups were broken, the intermediates lost a functional group that could adsorb on the surface of Sb₂S₃ and could not be further mineralized, which further demonstrated that the azo group was the group complexing with Sb₂S₃ in the photocatalytic process.

Fig. 11 shows the zeta potential measurement for A-Sb₂S₃. The natural pH value of A-Sb₂S₃ aqueous suspension was about 5.4 and the zeta potential was approximately -45 mV . Even if the pH was adjusted to 1, the point of zero charge (pH_{pzc}) could not be obtained. The results indicated that OH^- was strongly bonded to the coordinatively unsaturated Sb³⁺ [45] and that it was difficult to displace by general ligands [46].

However, the surface hydroxyls of A-Sb₂S₃ could be partially substituted by the azo group of MO, as demonstrated by ATR-FTIR experiments in D₂O (Fig. 12). The stretching vibration of the hydrogen-bonded MeO-D was 2480 cm^{-1} , while those of the hydrogen-bonded D₂O were 2400 and 1200 cm^{-1} [47,48]. When MO was added to the suspension, the intensity of the peaks became weaker, indicating that a portion of the surface hydroxyls was substituted by the azo groups of MO. And, since the zeta potential of A-Sb₂S₃ was -45 mV at the tested pH = 9, the negatively charged $-\text{SO}_4^{2-}$ group could not adsorb to the surface of A-Sb₂S₃ due to strong electrostatic repulsion, while the azo group exhibited a charge distribution with weaker polarity, thus avoiding electrostatic repulsion. The result indicated that the azo group displaced hydroxyl groups (OH^-) to complex with coordinatively unsaturated Sb³⁺ on the surface of A-Sb₂S₃ via σ bonding between the

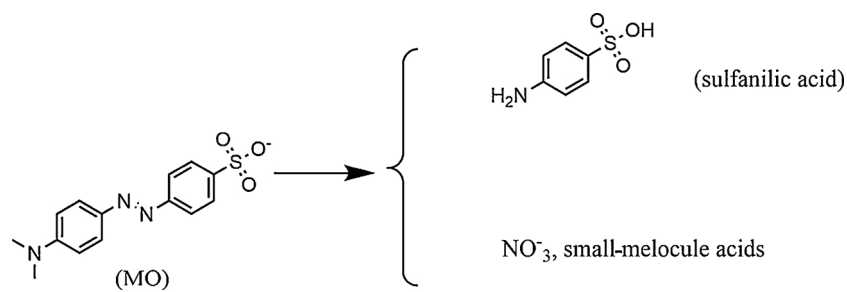


Fig. 9. Possible transformation pathways of MO in A-Sb₂S₃ aqueous solution under visible light irradiation.

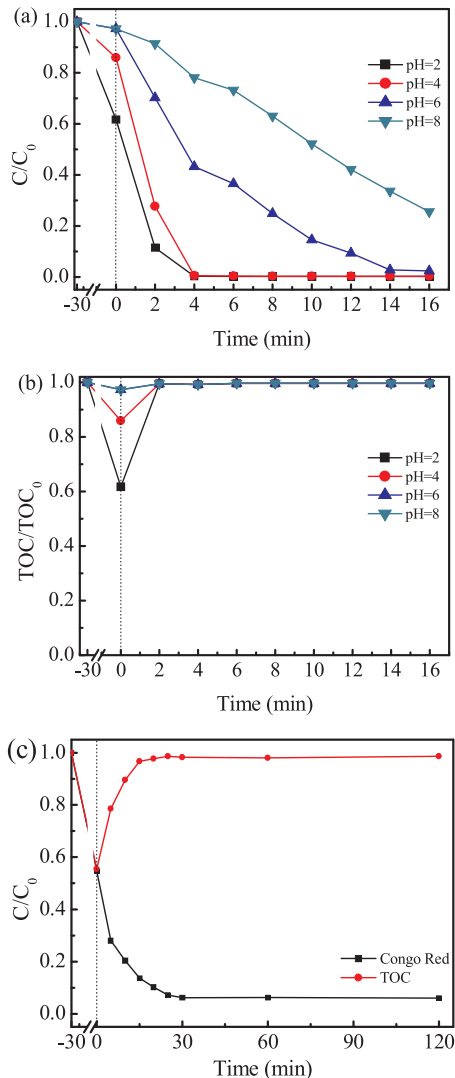


Fig. 10. (a) Degradation curves and (b) TOC removal curves of MO as a function of pH. Reaction conditions: $\lambda > 420 \text{ nm}$, light intensity $2.25 \text{ mW} \cdot \text{cm}^{-2}$, initial MO concentration 10 mg L^{-1} and catalyst (A-Sb₂S₃) concentration 1.0 g L^{-1} . (c) Photocatalytic degradation and TOC removal curve of Congo Red. (For interpretation of the references to colour in this figure legend, the reader is referred to the web version of this article).

lone pairs of nitrogen atoms in the azo group and Sb³⁺ ($\sigma\text{-Sb}-(-\text{N}=\text{N}-)$), causing the adsorption of MO/ Congo Red onto the surface of Sb₂S₃.

The complexation of the azo group with Sb³⁺ played an important role in the photoreaction, therefore adsorbed-MO, adsorbed-Congo Red, and bare A-Sb₂S₃ were made into working electrodes for transient photocurrent response tests (Fig. 13). As can be seen, the photocurrent

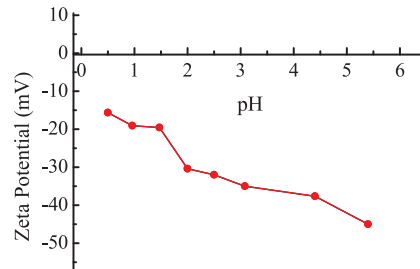


Fig. 11. Zeta potential as a function of pH for A-Sb₂S₃ suspension in the presence of KNO_3 (10^{-3} M).

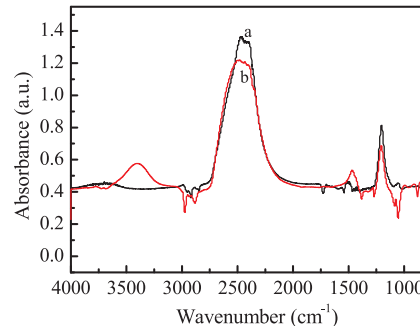


Fig. 12. ATR-FTIR spectra of A-Sb₂S₃ suspension in D_2O : (a) without MO, (b) with MO.

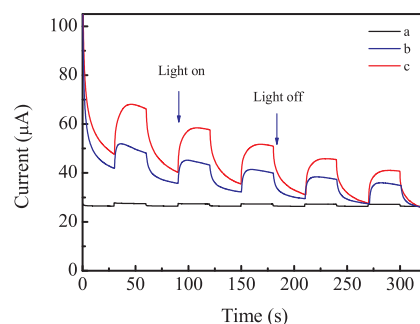


Fig. 13. The transient photocurrent response of (a) pure A-Sb₂S₃, (b) A-Sb₂S₃ adsorbed MO, (c) A-Sb₂S₃ adsorbed Congo Red under visible light. (For interpretation of the references to colour in this figure legend, the reader is referred to the web version of this article).

responses increased according to the following order: bare A-Sb₂S₃, adsorbed-MO A-Sb₂S₃, adsorbed-Congo Red A-Sb₂S₃. The result indicated that the strong complexation of OH⁻ with Sb³⁺ led OH⁻ to become a recombination center for photogenerated electrons and holes, while the complexation of azo groups with Sb³⁺ enhanced the separation and migration of photogenerated electron-hole pairs in A-Sb₂S₃ due to partial charge transfer between the azo group and Sb³⁺

[23].

No significant ·O[·] or ·OH radicals were determined by the ESR spin-trap technique (with BMPO) in dispersions of A-Sb₂S₃ under both dark conditions and visible light irradiation, indicating lower separation and migration of photogenerated electron and hole. Nevertheless, due to the partial charge transfer role of the complexes (σ -Sb(-N=N-)) between azo dyes and A-Sb₂S₃, photogenerated holes in the valence band of A-Sb₂S₃ transferred quickly to the azo group to oxidize -N=N- into NO[·] with the production of small-molecule acids. At the same time, the photogenerated electrons in the conduction band of A-Sb₂S₃ also transferred to the azo group to reduce -N=N-, producing sulfanilic acid. With the destruction of the azo group, these intermediates quickly desorbed from the surface of the catalyst into solution and were not oxidized any further. All the above results verified that the complexes (σ -Sb(-N=N-)) could transmit electrons and holes to the azo group, reducing/oxidizing and breaking the -N=N- bond, causing azo dye decolorization to improve biodegradability.

4. Conclusion

An amorphous Sb₂S₃ photocatalyst was successfully synthesized via a hydrothermal procedure by adjusting the concentration of hydrochloric acid. The visible-light driven photoactivity of amorphous Sb₂S₃ (A-Sb₂S₃) was nearly 13 times higher than that of the crystalline samples (C-Sb₂S₃-1 and C-Sb₂S₃-2). The predominant decolorization pathways of MO were reduction and oxidation of its azo group, producing sulfanilic acid, NO₃[·] and small-molecule acids, and the breakage of the -N=N- bond improved the biodegradability of the MO solution. Moreover, the photocatalytic activity was positively correlated with the adsorption capacity of MO on A-Sb₂S₃. It was proposed that the formed complexes (σ -Sb(-N=N-)) could transmit photogenerated electrons and holes to the azo group, breaking the -N=N- bond, causing azo dye decolorization to improve biodegradability. These results may provide a vital insight for pollutant degradation via constructing a complex between the catalyst and pollutant.

Acknowledgments

This work was supported by the National Key Research and Development Plan (2016YFA0203200), National Natural Science Foundation of China (51538013) and the Science Starting Foundation of Guangzhou University (27000503151 and 2700050302).

References

- [1] H. Lachheb, E. Puzenat, A. Houas, M. Ksibi, E. Elaloui, C. Guillard, J.-M. Herrmann, Photocatalytic degradation of various types of dyes (Alizarin S, Crocein Orange G, Methyl Red, Congo Red, Methylene Blue) in water by UV-irradiated titania, *Appl. Catal. B* 39 (2002) 75–90.
- [2] C. Hu, Y. Wang, H. Tang, C. Hu, Y. Wang, H. Tang, Preparation and characterization of surface bond-conjugated TiO₂/SiO₂ and photocatalysis for azo dyes, *Appl. Catal. B* 30 (2001) 277–285.
- [3] Y. Huang, W. Fan, B. Long, H. Li, F. Zhao, Z. Liu, Y. Tong, H. Ji, Visible light Bi₂S₃/Bi₂O₃/Bi₂O₃CO₃ photocatalyst for effective degradation of organic pollutions, *Appl. Catal. B* 185 (2016) 68–76.
- [4] S. Zhang, J. Li, X. Wang, Y. Huang, M. Zeng, J. Xu, Rationally designed 1D Ag@AgVO₃ nanowire/graphene/protonated g-C₃N₄ nanosheet heterojunctions for enhanced photocatalysis via electrostatic self-assembly and photochemical reduction methods, *J. Mater. Chem. A* 3 (2015) 10119–10126.
- [5] J. He, D.W. Shao, L.C. Zheng, L.J. Zheng, D.Q. Feng, J.P. Xu, X.H. Zhang, W.C. Wang, W.H. Wang, F. Lu, H. Dong, Y.H. Cheng, H. Liu, R.K. Zheng, Construction of Z-scheme Cu₂O/Cu/AgBr/Ag photocatalyst with enhanced photocatalytic activity and stability under visible light, *Appl. Catal. B* 203 (2017) 917–926.
- [6] W.J. Ong, L.L. Tan, Y.H. Ng, S.T. Yong, S.P. Chai, Graphitic carbon nitride (g-C₃N₄)-Based photocatalysts for artificial photosynthesis and environmental remediation: are we a step closer to achieving sustainability? *Chem. Rev.* 116 (2016) 7159–7329.
- [7] A. Etogo, E. Hu, C. Zhou, Y. Zhong, Y. Hu, Z. Hong, Facile fabrication of mesoporous BiOCl/(BiO)₂CO₃/Bi₂O₃ ternary flower-like heterostructured microspheres with high visible-light-driven photoactivity, *J. Mater. Chem. A* 3 (2015) 22413–22420.
- [8] H. Sheng, H. Zhang, W. Song, H. Ji, W. Ma, C. Chen, J. Zhao, Activation of water in titanium dioxide photocatalysis by formation of surface hydrogen bonds: an in situ IR spectroscopy study, *Angew. Chem. Int. Ed. Engl.* 54 (2015) 5905–5909.
- [9] C. Yu, W. Zhou, H. Liu, Y. Liu, D.D. Dionysiou, Design and fabrication of microsphere photocatalysts for environmental purification and energy conversion, *Chem. Eng. J.* 287 (2016) 117–129.
- [10] V. Kostas, M. Baikousi, K. Dimos, K.C. Vasilopoulos, I. Koutselas, M.A. Karakassides, Efficient and rapid photocatalytic reduction of hexavalent chromium achieved by a phloroglucinol-derived microporous polymeric organic framework solid, *J. Phys. Chem. C* 121 (2017) 7303–7311.
- [11] D. Wu, S. Yue, W. Wang, T. An, G. Li, H.Y. Yip, H. Zhao, P.K. Wong, Boron doped Bi₂O₃ nanosheets with enhanced photocatalytic inactivation of Escherichia coli, *Appl. Catal. B* 192 (2016) 35–45.
- [12] R. Asahi, T. Morikawa, H. Irie, T. Ohwaki, Nitrogen-doped titanium dioxide as visible-light-sensitive photocatalyst: designs, developments, and prospects, *Chem. Rev.* 114 (2014) 9824–9852.
- [13] Y. Huang, H. Li, M.-S. Balogun, W. Liu, Y. Tong, X. Lu, H. Ji, Oxygen vacancy induced bismuth oxyiodide with remarkably increased visible-light absorption and superior photocatalytic performance, *ACS Appl. Mater. Interfaces* 6 (2014) 22920–22927.
- [14] Y. Huang, K. Li, Y. Lin, Y. Tong, H. Liu, Enhanced efficiency of electron–hole separation in Bi₂O₂CO₃ for photocatalysis via acid treatment, *ChemCatChem* 10 (2018) 1982–1987.
- [15] C. Yu, L. Wei, W. Zhou, J. Chen, Q. Fan, H. Liu, Enhancement of the visible light activity and stability of Ag₂CO₃ by formation of AgI/Ag₂CO₃ heterojunction, *Appl. Surf. Sci.* 319 (2014) 312–318.
- [16] Y. Huang, H. Xu, H. Yang, Y. Lin, H. Liu, Y. Tong, Efficient charges separation using advanced BiOI-based hollow spheres decorated with palladium and manganese dioxide nanoparticles, *ACS Sustain. Chem. Eng.* 6 (2018).
- [17] H. Shi, G. Li, H. Sun, T. An, H. Zhao, P.-K. Wong, Visible-light-driven photocatalytic inactivation of E. Coli by Ag/AgX-CNTs (X = Cl, Br, I) plasmonic photocatalysts: bacterial performance and deactivation mechanism, *Appl. Catal. B* 158–159 (2014) 301–307.
- [18] Y.-H. Chiu, Y.-J. Hsu, Au@Cu₂S₄ yolk@shell nanocrystal-decorated TiO₂ nanowires as an all-day-active photocatalyst for environmental purification, *Nano Energy* 31 (2017) 286–295.
- [19] R. Shi, Y. Wang, D. Li, J. Xu, Y. Zhu, Synthesis of ZnWO₄ nanorods with [100] orientation and enhanced photocatalytic properties, *Appl. Catal. B* 100 (2010) 173–178.
- [20] R. Li, H. Han, F. Zhang, D. Wang, C. Li, Highly efficient photocatalysts constructed by rational assembly of dual-cocatalysts separately on different facets of BiVO₄, *Energy Environ. Sci.* 7 (2014) 1369–1376.
- [21] D. Liu, W. Cai, Y. Wang, Y. Zhu, Constructing a novel Bi₂SiO₅/BiPO₄ heterostructure with extended light response range and enhanced photocatalytic performance, *Appl. Catal. B* 236 (2018) 205–211.
- [22] Y. Zhou, Y. Zhang, M. Lin, J. Long, Z. Zhang, H. Lin, J.C. Wu, X. Wang, Monolayered Bi₂WO₆ nanosheets mimicking heterojunction interface with open surfaces for photocatalysis, *Nat. Commun.* 6 (2015) 8340.
- [23] A. Lagutchenkov, R.K. Sinha, P. Maitre, O. Dopfer, Structure and infrared spectrum of the Ag⁺-phenol ionic complex, *J. Phys. Chem. A* 114 (2010) 11053–11059.
- [24] L. Lyu, L. Zhang, Q. Wang, Y. Nie, C. Hu, Enhanced Fenton catalytic efficiency of gamma-Cu-Al²O³ by sigma-Cu²⁺-ligand complexes from aromatic pollutant degradation, *Environ. Sci. Technol.* 49 (2015) 8639–8647.
- [25] W. Lou, M. Chen, X. Wang, W. Liu, Novel single-source precursors approach to prepare highly uniform Bi₂S₃ and Sb₂S₃ nanorods via a solvothermal treatment, *Cheminform* 38 (2010) no-no.
- [26] E. Zimmermann, T. Pfadler, J. Kalb, J.A. Dorman, D. Sommer, G. Hahn, J. Weickert, L. Schmidt-Mende, Toward high-efficiency solution-processed planar heterojunction Sb₂S₃ solar cells, *Adv. Sci. (Weinh)* 2 (2015) 1500059.
- [27] C.-M. Park, Y. Hwa, N.-E. Sung, H.-J. Sohn, Stibnite (Sb₂S₃) and its amorphous composite as dual electrodes for rechargeable lithium batteries, *J. Mater. Chem.* 20 (2010) 1097–1102.
- [28] S.M. Hwang, J. Kim, Y. Kim, Na-ion storage performance of amorphous Sb₂S₃ nanoparticles: anode for Na-ion batteries and seawater flow batteries, *J. Mater. Chem. A Mater. Energy Sustain.* 4 (2016) 17946–17951.
- [29] H. Hou, M. Jing, Z. Huang, Y. Yang, Y. Zhang, J. Chen, Z. Wu, X. Ji, One-dimensional rod-like Sb₂S₃-based anode for high-performance sodium-ion batteries, *ACS Appl. Mater. Interfaces* 7 (2015) 19362–19369.
- [30] N. Balis, D. Konios, E. Stratakis, E. Kymakis, Ternary organic solar cells with reduced graphene Oxide-Sb₂S₃ hybrid nanosheets as the cascade material, *ChemNanoMat* 1 (2015) 346–352.
- [31] X.B. Cao, L. Gu, L.J. Zhuge, W.J. Gao, W.C. Wang, S.F. Wu, Template-free preparation of hollow Sb₂S₃ microspheres as supports for Ag nanoparticles and photocatalytic properties of the constructed metal–Semiconductor nanostructures, *Adv. Funct. Mater.* 16 (2006) 896–902.
- [32] J. Tang, J. Li, Y. Cheng, P. Huang, Q. Deng, Facile hydrothermal-carbonization preparation of carbon-modified Sb₂S₃ composites for photocatalytic degradation of methyl orange dyes, *Vacuum* 120 (2015) 96–100.
- [33] X. Shuai, W. Shen, A facile chemical conversion synthesis of Sb₂S₃ nanotubes and the visible light-driven photocatalytic activities, *Nanoscale Res. Lett.* 7 (2012) 199.
- [34] H. Wang, X. Yuan, H. Wang, X. Chen, Z. Wu, L. Jiang, W. Xiong, G. Zeng, Facile synthesis of Sb₂S₃/ultrathin g-C₃N₄ sheets heterostructures embedded with g-C₃N₄ quantum dots with enhanced NIR-light photocatalytic performance, *Appl. Catal. B* 193 (2016) 36–46.
- [35] Y. Liu, X. Yuan, H. Wang, X. Chen, S. Gu, Q. Jiang, Z. Wu, L. Jiang, Y. Wu, G. Zeng, Novel visible light-induced g-C₃N₄-Sb₂S₃/Sb₄O₅Cl₂ composite photocatalysts for efficient degradation of methyl orange, *Catal. Commun.* 70 (2015) 17–20.
- [36] J. Zhang, Z. Liu, Z. Liu, Novel WO₃/Sb₂S₃ heterojunction photocatalyst based on

WO₃ of different morphologies for enhanced efficiency in photoelectrochemical water splitting, *ACS Appl. Mater. Interfaces* 8 (2016) 9684–9691.

[37] A.V. Kozytskiy, O.L. Stroyuk, M.A. Skoryk, V.M. Dzhagan, S.Y. Kuchmiy, D.R.T. Zahn, Photochemical formation and photoelectrochemical properties of TiO₂/Sb₂S₃ heterostructures, *J. Photochem. Photobiol. A* Chem. 303–304 (2015) 8–16.

[38] L. Zhang, C. Hu, H. Ji, p-AgI anchored on {001} facets of n-Bi₂O₂CO₃ sheets with enhanced photocatalytic activity and stability, *Appl. Catal. B* 205 (2017) 34–41.

[39] M.A. Butler, Photoelectrolysis and physical properties of the semiconducting electrode WO₂, *J. Appl. Phys.* 48 (1977) 1914–1920.

[40] J. Tauc, Absorption edge and internal electric fields in amorphous semiconductors, *Mater. Res. Bull.* 5 (1970) 721–729.

[41] P. Qiu, C. Xu, H. Chen, F. Jiang, X. Wang, R. Lu, X. Zhang, One step synthesis of oxygen doped porous graphitic carbon nitride with remarkable improvement of photo-oxidation activity: role of oxygen on visible light photocatalytic activity, *Appl. Catal. B* 206 (2017) 319–327.

[42] C. Galindo, P. Jacques, A. Kalt, Photodegradation of the aminoazobenzene acid orange 52 by three advanced oxidation processes: UV/H₂O₂, UV/TiO₂ and VIS/TiO₂: comparative mechanistic and kinetic investigations, *J. Photochem. Photobiol. A* Chem. 130 (2000) 35–47.

[43] J. Fan, Y. Guo, J. Wang, M. Fan, Rapid decolorization of azo dye methyl orange in aqueous solution by nanoscale zerovalent iron particles, *J. Hazard. Mater.* 166 (2009) 904–910.

[44] P. Li, Y. Song, S. Wang, Z. Tao, S. Yu, Y. Liu, Enhanced decolorization of methyl orange using zero-valent copper nanoparticles under assistance of hydrodynamic cavitation, *Ultrason. Sonochem.* 22 (2015) 132–138.

[45] J. Nawrocki, M. Rigney, A. McCormick, P.W. Carr, Chemistry of zirconia and its use in chromatography, *J. Chromatogr. A* 657 (1993) 229.

[46] B. Kasprzyk-Hordern, Catalytic ozonation and methods of enhancing molecular ozone reactions in water treatment, *Appl. Catal. B Environ.* 46 (2003) 639–669.

[47] J. Bing, C. Hu, Y. Nie, M. Yang, J. Qu, Mechanism of catalytic ozonation in Fe₂O₃/Al₂O₃@SBA-15 aqueous suspension for destruction of ibuprofen, *Environ. Sci. Technol.* 49 (2015) 1690–1697.

[48] A. Lv, C. Hu, Y. Nie, J. Qu, Catalytic ozonation of toxic pollutants over magnetic cobalt and manganese co-doped γ-Fe₂O₃, *Appl. Catal. B* 100 (2010) 62–67.